ANNALS OF GEOPHYSICS, 67,1, SE109, 2024; doi.10.4401/ag-8984
OPEN ACCESS

Understanding the structure of crust and shallow upper mantle beneath western Tibet through the joint inversion of Rayleigh wave group velocity dispersion with interpolated receiver functions

Ritima Das[1], Utpal Saikia[*,2], Gokul Kumar Saha[3]

(1) Department of Earth Sciences, PondicherryUniversity, Pondicherry, 605014, India
(2) Department of Earth & Climate Science, Indian Institute of Science Education & Research- Tirupati, Tirupati-517507, India
(3) Department of Earth and Climate Science, Indian Institute of Science Education & Research- Pune, Dr. Homi Bhabha Road, Pune-411008, India

Article history: received Mary 30, 2023; accepted February 6, 2024

Abstract

We present the 3-D shear wave velocity variationin the crust and upper mantle structure of western Tibet using a joint inversion of Rayleigh wave group velocity dispersion and interpolated receiver function. The lateral sampling of the receiver function and the surface wave dispersion is equalized by the interpolation scheme. This new method of spatial interpolation eliminates difficulties caused by back azimuthal variation in the receiver function. We have jointly inverted these interpolated receiver functions with the Rayleigh wave group velocity dispersions obtained from the earthquake and ambient noise tomography to map the tectonic structure of western Tibet. The study reveals remarkable variation of the seismic characteristics in the crust and shallow upper mantle of western Tibet. The mapped Moho depth is ~74 km in the northern part of the plateau, whereas it is ~69 km in the southern part. A thick mid-crustal slow-velocity zone from ~10km up to ~40 km depth has been observed, which could be attributed to partial melt. A noteworthy finding is the variation in slower crustal velocity between the south and north of the Lhasa Block (LB). We interpret this as the Indian crust that has been underthrusted beneath the Tibetan plateau, and the northern limit of the Indian lithosphere extends to the southern part of the LB.

Keywords: Himalaya; Tibet; Receiver Function; Joint Inversion; Moho depth; Mid crustal slow-velocity

1. Introduction

The Tibetan plateau, comprising an area of ~2.5 million km^2 with an average elevation of 4500 m, is believed to be the largest and highest plateau on the Earth. The Himalaya-Tibet orogen is an ideal place to study active continent-continent collision. So far, several decades of studies have been conducted to understand the tectonic

diversity beneath the Himalaya and Tibet, but numerous debates on this topicare still ongoing.Furthermore, several tectonic models have been proposed to explain the growth and formation of Tibetan plateau [Allegre et al., 1984; England and Houseman, 1986; Ni and Barazangi, 1984; Beaumont et al., 2001; Tilman et al., 2003; Rai et al., 2006]. The collision between India and Asia has been continuously progressing from the Late Cretaceous to the Early Paleocene. This process leads to the obduction of ophiolites onto the passive continental margin of the Indian plate and the initial contact between the crust of India and Eurasia. The entire collision process resulted in the withdrawal of the Tethyan Ocean by depositing marine sediments in the Indus-Yarlung Suture (IYS) [Green et al., 2008; Searle et al., 2011]. Other main significant consequences of this collision include the significant increase in the thickness of the crust and the occurrence of massive earthquakes at the periphery of the Tibetan plateau [Bilham, 2004]. The deformation history of Tibetan Plateau is illuminated by several models [Argand 1924; Godin et al., 2006; England and McKenzie, 1982, 1983; England and Houseman, 1985; Law et al., 2004, 2006;Molnar and Tapponnier, 1975; Tapponnier and Molanr, 1976, 1977; Tapponnier et al., 1982; Royden et al., 1997; Searle et al., 2003, 2006].

Despite numerous experiments conducted to comprehend the tectonic structure of the Himalayas and Tibet, further investigations are required to acquire a comprehensive understanding of the evolutionary processes involved. Many debates still remain in understanding the behaviour of Tibetan lithosphere. One among these is whether the Indian lithosphere is underthrusting beneath Tibetan crust, which could potentially account for the primary cause behind the crustal thickening of the plateau [Kosarev et al., 1999; Li et al., 2008]. Next is the fate of the Indian crust. It remains unknown to what extent the Indian lithosphere can be found under Tibetan plateau or whether it has been transformed into eclogite, a higher density metamorphic rock[Huang et al., 2009; Nabelek et al., 2009; Razi et al., 2016]. Furthermore, some studies explain the possibility of material flowing from Tibet into the Himalaya as a result of mid-to-lower crustal channel flow [Copley and McKenzie, 2007; Gilligan et al., 2015; Royden et al., 2008; Searle et al., 2011].

In this paper, we investigate the crust and uppermost mantle structure (down to 130 km depth) beneath western Tibet using the joint inversion of receiver function and Rayleigh wave group velocity dispersion. Here, we utilize a new interpolation scheme to calculate receiver functions, which enhances our understanding of the dynamic structure beneath the region. The interpolated receiver functions yield a simpler velocity model, particularly enabling us to overcome the challenges posed by poorly sampled back azimuthal variations. The method also aids in equalizing the lateral sensitivity of the receiver functions and the surface wave dispersions. We provide a detailed description of the method in section 3, contributing to our comprehensionof the dynamic tectonic structure beneath Tibetan plateau.

2. Geological settings and previous studies of the lithospheric structure

The study region comprises the Himalaya, the Lhasa Block (LB), and the Qiangtang Block (QB) (Fig. 1). In the south, it is comprised of the Karakorum Fault (KKF), which is believed to have initiated between 18 and 11 million years ago [Murphy et al., 2000; Searle et al., 1998], and the IYS in the Himalayan region. Towards the north is the LB, which is bounded by the IYS in the south. The shape of this block is narrow in the west and widens towards the east. The LB is separated from the QB in the north by a ~1200 km east-west trending zone called Bangong-Nujiang-Suture (BNS).

The shape of the QB is approximately 500-600 km wide in the central part and narrows down (<150 km) towards the west. Towards the west, it elongates to the KKF [Yin and Harrison, 2000]. Thus, the study region comprises a section from both the India plate and Eurasian plate. The predominantly exposed, deep metamorphic rocks found in the region are considered to have formed in Cenozoic ages [Matte et al., 1996]. The LB and the QB have different histories of tectonic settings [Yin and Harrison, 2000]. Searle et al. [2011] described that the eruptions of the Potassic-ultrapotassic shoshonitic and adakitic lavas everywhere on the QB (50-29 Ma) and the LB (30-10 Ma), indicating a hot mantle, thick crust, and eclogitic root during that time. The timing of the final assemblage of all the blocks of Tibetan plateau is always debatable; however, a broadly acceptable period is ~50 Myr [Yin and Harrison, 2000]. The thickening and shortening of the crust of Tibetan plateau occurred before and after the collision between India and Asia, according to Searle et al. (2011].

The lithospheric deformation of Tibetan plateau has been described with various geodynamic models, such as underthrusting, rigid block, continuum, and channel, among others. The underthrusting model for Tibet was proposed by Argand [1924]. It states that the crustal thickening in Tibet is a result of the underthrusting of the

entire plateau by the Indian plate. Several studies have proposed a rigid block, which suggests that the Tibetan crust could be regarded as a rigid-plastic medium notched by the rigid Indian plate [Avouac and Tapponnier, 1993; Molnar and Tapponnier, 1975; Tapponnier and Molnar, 1976, 1977]. England and McKenzie [1982; 1983] proposed the continuum model, which states that the deformation of the continental lithosphere over the long term, on a bulk scale, is a continuum with Newtonian or power law rheology. Royden et al. [1997; 2008] proposed the crustal flow model of lower crust, which defines that the lower crust is generally weaker and appears to be a distinct layer between the upper crust and upper mantle. The channel flow model suggests that a partially molten middle crust was forced under the Greater Himalaya during the early Miocene [Godin et al., 2006; Grujic et al., 2002; Searle and Rex, 1989; Searle and Szulc, 2005; Searle et al., 2003, 2006]. These models describe the various possible mechanisms that led to the deformation of Tibetan plateau's crust.

In order to gain a better understanding of crustal and shallow upper mantle structure and its behavior underneath western Tibet, numerous studies have been conducted so far. These studies encompass a range of approaches, including refraction analysis [Zhang et al., 2011], receiver function investigations [Gilligan et al., 2015; Wittlinger et al., 2004), analysis of seismic wave travel times [Basuyau et al., 2013; Griffin et al., 2011; Nabelek et al., 2009], and surface wave studies [Caldwell et al., 2009; Rapine et al., 2003; Sun et al., 2010]. The collective findings consistently demonstrate that the crustal thickness beneath the western part of the Tibetan Plateau varies between 70 and 75 km. Moreover, measurements indicate compressional wave velocities (Vp) ranging from 6.0 to 6.4 km/s, while shear wave velocities (Vs) span the range of 3.2 to 3.6 km/s [Caldwell et al., 2009; Razi et al., 2014; Sun et al., 2010; Yang et al., 2010]. Underthrusting of the Indian lithosphere beneath the Tibetan plateau has been observed in several studies [Basuyau et al., 2013; Huang et al., 2009; Kosarev et al., 1999; Li et al., 2008; Nabelek et al., 2009; Ni and Barazangi, 1984; Rai et al., 2006; Razi et al., 2014; Tilmann et al., 2003]. All of the above studies inferred the presence of eclogite in the lower crust of the Indian plate under the Greater Himalaya, as well as in the southern part of the Tibetan plateau. Additionally, a number of studies have also observed a mid-crustal slow-velocity zone beneath western Tibet [Bao et al., 2015; Caldwell et al., 2009; Cotte et al., 1999; Gilligan et al., 2015; Rapine et al., 2003]. This raises two questions in the region: whether there is a slow velocity zone within the middle crust or whether eclogites exist in the lower crust of India beneath the Greater Himalaya and Tibet. Overall, the debate regarding the lithospheric structure beneath Tibet remains ongoing. Employing a combined analysis of Rayleigh wave group velocity dispersion and interpolated receiver function, the examination of crust and uppermost mantle structure potentially offers an effective method to address this issue.

3. Data and Method

This study used the data from a seismic experiment in western Tibet, which took place from 2007 to 2011. The experiment was conducted jointly by the United States and China (known as the Y2 array). The seismic network was distributed in the western part of Tibetan Plateau (Fig. 1a). The station spacing was approximately 40-100 km. It consisted of 30 Streckeisen STS-2 seismometers, recorded by Quanterra Q330 acquisition system at 100 samples per second. The recordings were time-corrected using GPS time. The seismographs were deployed in two phases: 10 stations operated from 2007 to 2011, and an additional 20 stations operated from 2009 to mid-2011. The region covered includes a part of KKF, IYS and BNS. We used this data set for constructions the receiver functions. For the surface wave dispersion, we extracted values from the surface wave tomography for the entire south Asia using ambient noise and earthquake data [Saha et al., 2020;2021]. We provide a brief overview of the surface wave dispersion and the receiver functions that were used for the inversion.

3.1 Surface wave dispersions

The group velocities of fundamental mode Rayleigh wave have been computed for the entire Indian shield, including the Himalaya and Tibet. We utilized Multiple Filter Technique (MFT) method developed by Dziewonski et al. [1969], and later improved by Herrmann [1973], Bhattacharya [1983], Herrmann and Ammon [2004]. The group velocity dispersions were calculated for both the cross-correlation of ambient noise data and earthquake data. The seismological data recorded at 683 seismic stations were used to compute the cross-correlation of ambient noise (Fig. S1a). Continuous vertical component seismograms were used to compute the cross-correlation

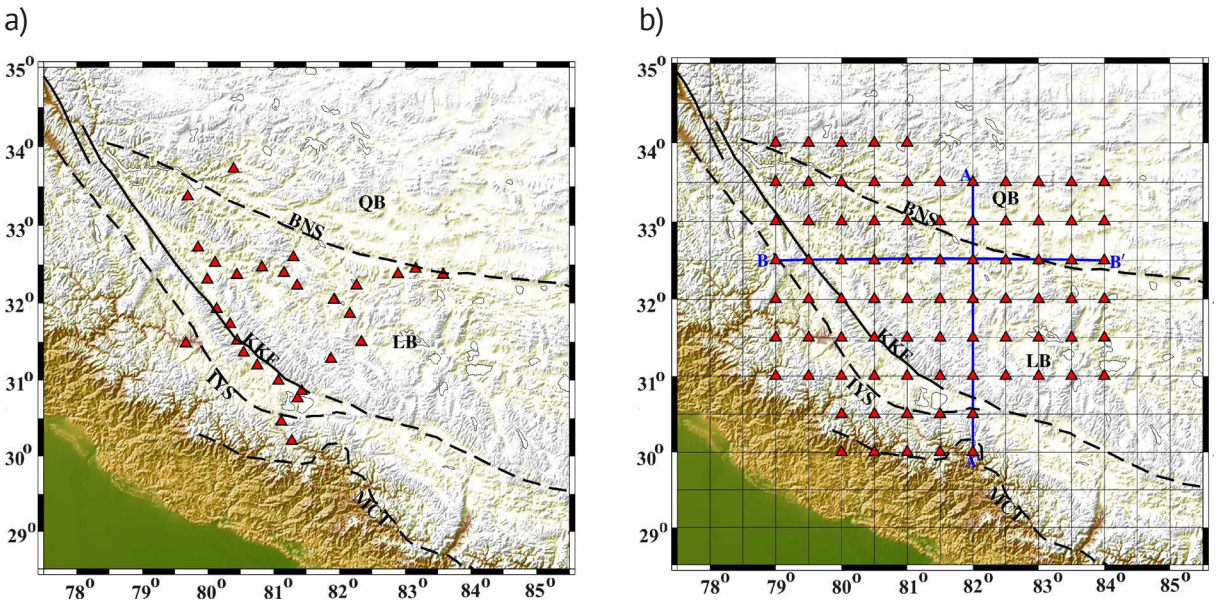

Figure 1. (a) The tectonic map of Western Tibet along with station location (red triangles) used in the receiver function (RF) interpolation. Major geological features are represented with QB (Qiangtang Block), LB (Lhasa Block), BNS (Bangong-Nujiang Suture), KKF (Karakorum Fault) and IYS (Indus-Yarlung Suture). (b) Map of evenly sampled grid cells used for receiver function interpolation. Each triangle represents a seismic station where the stacked RFs have been computed. The profile AA′ and BB′ are shown, along which the velocity cross-sections are plotted in Figure 8.

[Bensen et al., 2007]. A total of 18,552 paths were used to calculate the cross-correlation of the ambient noise. Data recorded for identical dates were cross correlated for 24 hours long records to generate the pair-wise cross correlation function. Figure S2 illustrates the Rayleigh wave cross correlation at station WT01 in western Tibet. The cross-correlated functions obtained for each pair of stations are then averaged to generate a symmetric signal and stacked to improve the signal to noise ratio (SNR). The SNR is calculated by dividing the maximum absolute in the signal window by the standard deviation of the noise. For the final selection of the data, we have used only those cross correlation functions whose SNR is greater than 15, and inter station separation is equals to or greater than 3 times the wavelength [Lin et al., 2008]. The ray path distributions of the selected final data are shown in Fig. S1b. We then applied the multiple filter taper analysis to each noise correlation function to measure the group velocities. Next, we added group velocities along 3048 paths spanning the region obtained from the 417 earthquakes (with magnitude >5.5) recorded at 209 seismic stations. We chose the regional earthquakes between 15°S to 40°N and 31° to 130°E, with depths varies from 10 km to 95 km (Fig. S3a). The ray path coverage has been improved by adding these earthquake paths (Fig. S3b). The ray path distribution is for periods ranging from 5 s to 70 s, averaged for every 1° × 1° of the study region. An example of the stacked symmetric cross-correlation function and corresponding group velocity dispersion for both the inter-station cross-correlation function and the earthquake source is presented in Fig. 2. The details of the data are published in Saha et al. [2020; 2021].

3.2 Rayleigh wave group velocity tomography and resolution test

The Rayleigh wave group velocities along all source-receiver paths for each period are converted to group velocity maps. We construct 2D group velocity map for each period by using the methodology of Barmin et al. [2001]. Saha et al. [2021] provide a detailed presentation of the method applied to these sets of data. Figure S4 shows the Rayleigh wave group velocity maps at different periods: 5 s, 10 s, 30 s, and 70 s for the entire south Asia. In order to check the resolution of the group velocity maps, we used two different methods: the spike perturbation method [Barmin et al., 2001] and the checkerboard resolution test [Rawlinson and Spakman, 2016]. In the spike resolution test, the spatially distributed response of an impulsive input at a node is inverted to test the fidelity of the resolution

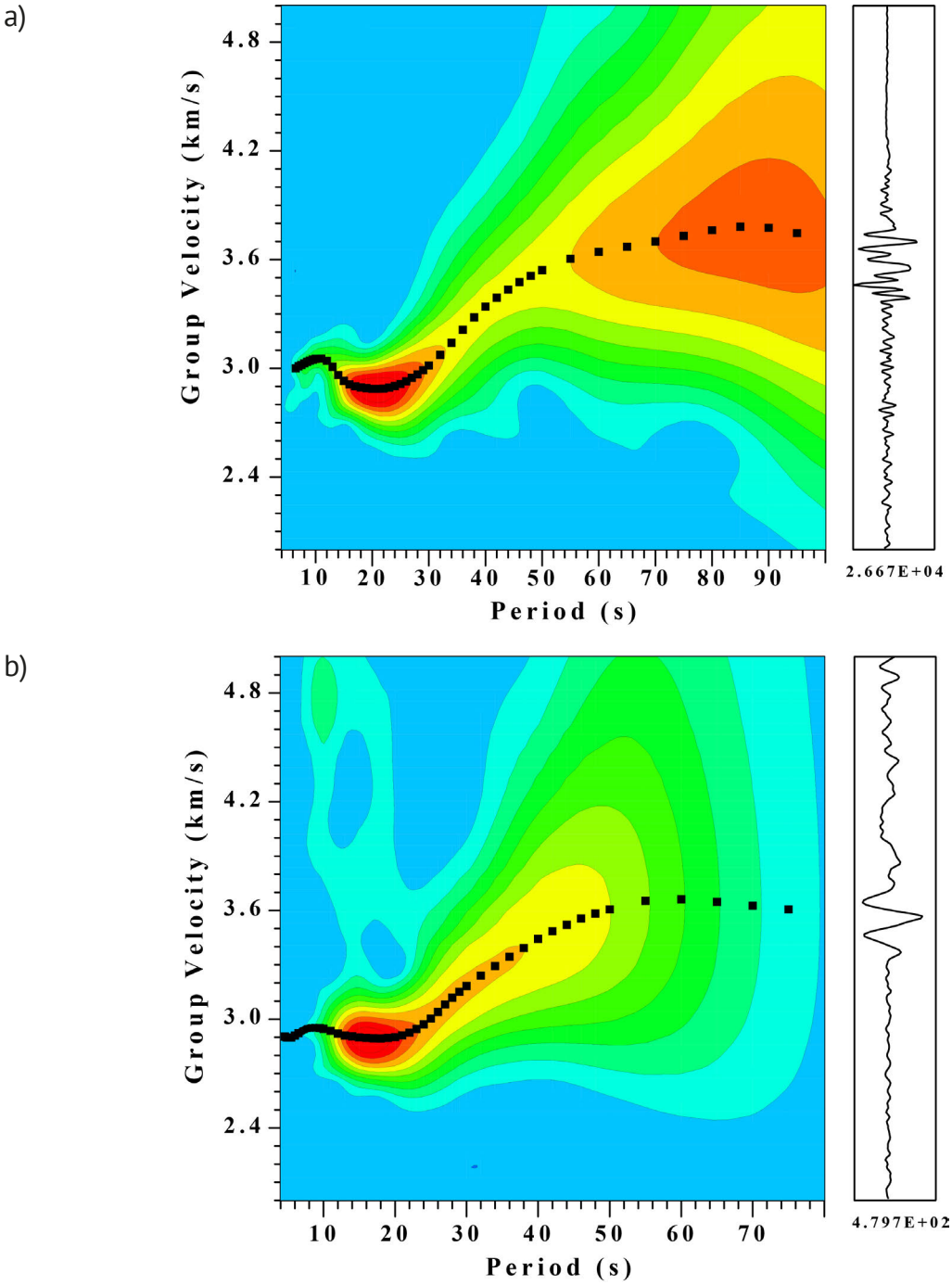

Figure 2. Rayleigh wave group velocity Vs Period for (a) The earthquake source and (b) The inter-station cross-correlation function from ambient noise. Background colour indicates the spectral amplitude and group velocities are shown in blue lines. The corresponding Green's functions are shown in the right hand side of the figure.

matrix by fitting the output to the Gaussian form of the spike. The width of the spike provides a measure of the resolution. From this test, we can see the resolution of approximately 100-200 km for periods ranging from 5 s to 70 s in our study region (Fig. S5). Next, we applied the checkerboard resolution test to evaluate the resolution of the tomography. Velocity perturbations of ±6% are assigned to cell sizes of 1° and 2°. The resolution of the ray paths used for this analysis for a given time period can be estimated by the distinctness with which the original pattern is reproduced in the inverted model. Figure S6 shows that a cell size of 1° × 1° offers the highest resolution for the data utilized in this study for periods ranging from 5 s to 70 s. Hence, based on the aforementioned tests, it is evident that the group velocity maps of the fundamental mode Rayleigh waves are well resolved at 1° × 1° using the data employed in this study for the western Tibet region.

3.3 Receiver Function (RF)

The receiver function (RF) is a routinely used method to extract the information of the interior of the Earth. Here, we used the iterative deconvolution algorithm [Ligorria and Ammon, 1999] in time domain for computing the RFs. The RFs are computed with Gaussian width 1.6 which corresponds to the frequency ~0.8 Hz. We have selected the earthquake data recorded for the epicentral distance 30° to 95° and with magnitude greater than 5.5 for the computation of the RFs. For further analysis, we have kept only those RFs whose signal to noise ratio (S/N) is greater than 8 and the convolution misfit of the radial component signal power is greater than 80%. The S/N of the RF is evaluated using a least squares misfit approach on the original radial waveform. In the misfit criteria, original radial waveform is compared with newly constructed radial waveform. In order to equalize the lateral sampling, we have interpolated the RFs. Chai et al. [2015] has explained in detail the scheme of RF interpolation for the dataset at western US (transportable array TA) and adjacent Canada (Canadian Rockies and Alberta network, Y5) and Mexico (Batholith Broadband network XY). They have explained in details about how the interpolation scheme can be used to extract the average responses for both the wider (TA) and smaller networks (XY and Y5). For the interpolation process, we utilized a sample grid spacing of 0.5° (Fig. 1b). At each grid point, we implemented station binning, which involved three bins based on ray parameter ranges. These ranges were set as 0.07 s/km, 0.05 to 0.07 s/km, and less than 0.05 s/km. The purpose of station binning was to ensure equal consideration of nearby stations and account for any variations in the number of observations available at each station.

We have used the sample grid spacing of 0.5° for the interpolation (Fig. 1b). For each grid point, we have considered three bins with ray parameter ranges 0.07 s/km, 0.05 to 0.07 s/km, and less than 0.05 s/km. Station binning equalizes the importance of the nearby stations, accounting for differences in the number of observations at each station. The available RFs at the seismic stations near to the grid point are binned according to the mentioned ray parameter ranges. Then, for each ray parameter range, we have constructed the RFs by taking the weighted stack average of all the waveforms in each bin, considering the grid point as the centre. We have chosen the distance range of d_1 and d_2 to be 50 km and 100 km, respectively, within which the weights of individual RFs are assigned. The weight given to the signals recorded within the distance d_1 from the grid point is 1. The weight decreases linearly from 1.0 to 0.0 with increasing distance from d_1 to d_2. When RFs are densely sampled over a region of stations, the interpolation method enables us to obtain measurements of the RFs at any place of interest in the region. This also provides a good azimuthal coverage of the region and, thus, yields a clearer structural image beneath the region.

As the maximum station spacing of the study region is 100 km, we have used d_2 as 100 km, which allows us to have data from 5-12 stations located within d_2. The interpolation of the receiver functions significantly increases the signal-to-noise ratio. Figure 3 presents the stacked RFs and interpolated RFs for the study region to assess their quality of interpolated RF. The interpolation of the RF makes it simplified and smooth. The final output after the interpolation enhances the arrivals, most likely associated with the crust-mantle transition. The method also helps to overcome the poorly sampled back azimuthal variation. Often, we are unable to obtain sufficient back azimuthal coverage of the data. The earthquake location used in this study is shown in Fig. S7. It is clear from the figure that we do not have sufficient data from the northwest and southwest directions. However, by performing the interpolation of the receiver functions, we could get the location points in almost all direction of the region. Thus, we can overcome the back azimuthal coverage problem by using the interpolated receiver functions.

3.4 Joint Inversion

We have used joint inversion of the RF (described in section 3.3) and surface wave dispersion (described in section 3.1 & 3.2) to obtain the shear wave velocity structure beneath western Tibet. The iterative linearized damped least square method by Julia et al. [2000] has been used for the inversion. The method states to minimize the following function S:

$$S = \frac{1-p}{N_r}\sum_{i=0}^{N_r}\left(\frac{O_{ri}-P_{ri}}{\sigma_{ri}}\right)^2 + \frac{p}{N_s}\sum_{j=0}^{N_s}\left(\frac{O_{sj}-P_{sj}}{\sigma_{sj}}\right)^2 \quad (1)$$

Given the following variables: N_r (Total numbers of receiver functions), N_s (Total numbers of surface wave dispersions), O_{ri} (Observed receiver function at time t_i), P_{ri} (Predicted receiver functions at time t_i), O_{sj} (j^{th} observed

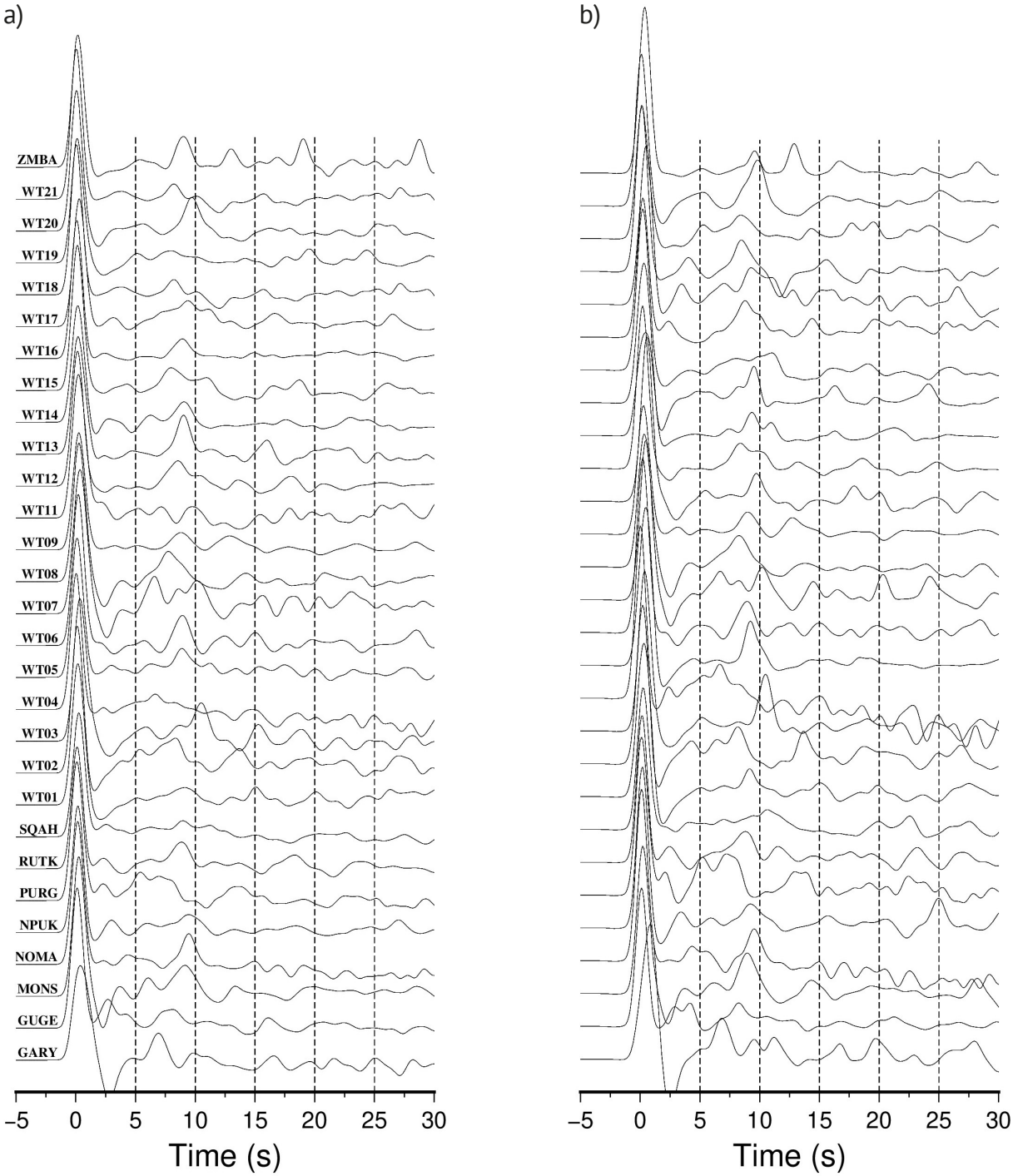

Figure 3. Stacked (left panel) and interpolated RFs for stations at western Himalaya and Tibet. Using weights based on the distance from each station, the interpolated RFs were calculated using the binned RFs within 100 km of the station.

surface wave dispersion), P_{sj} (j^{th} predicted surface wave dispersion), σ_{ri} (the standard errors in receiver function data set), and σ_{sj} (the standard errors in surface wave dispersion data set).

In the minimization procedure, an influence parameter, the factor '*p*' is an a priori value that changes the influence of either data set. The numerical value of '*p*' lies in between 0 to 1. Here, we have chosen a value of 0.5, which offers equal weightage to both datasets. For the initial velocity model, we have considered a half space model with a shear wave velocity 4.5 km/s (Vp/Vs = 1.73 and density = 3.3 g/cc) down to a depth of 130 km. We achieved convergence of the inversion model in 10 iterations. We performed the inversion for each ray parameter range of RF at the grid points. Each step of the inversion is performed for all the three ray parameter ranges of the RFs, and the final shear wave velocity model is measured as the average of all the models obtained from the three bins of the ray parameter ranges.

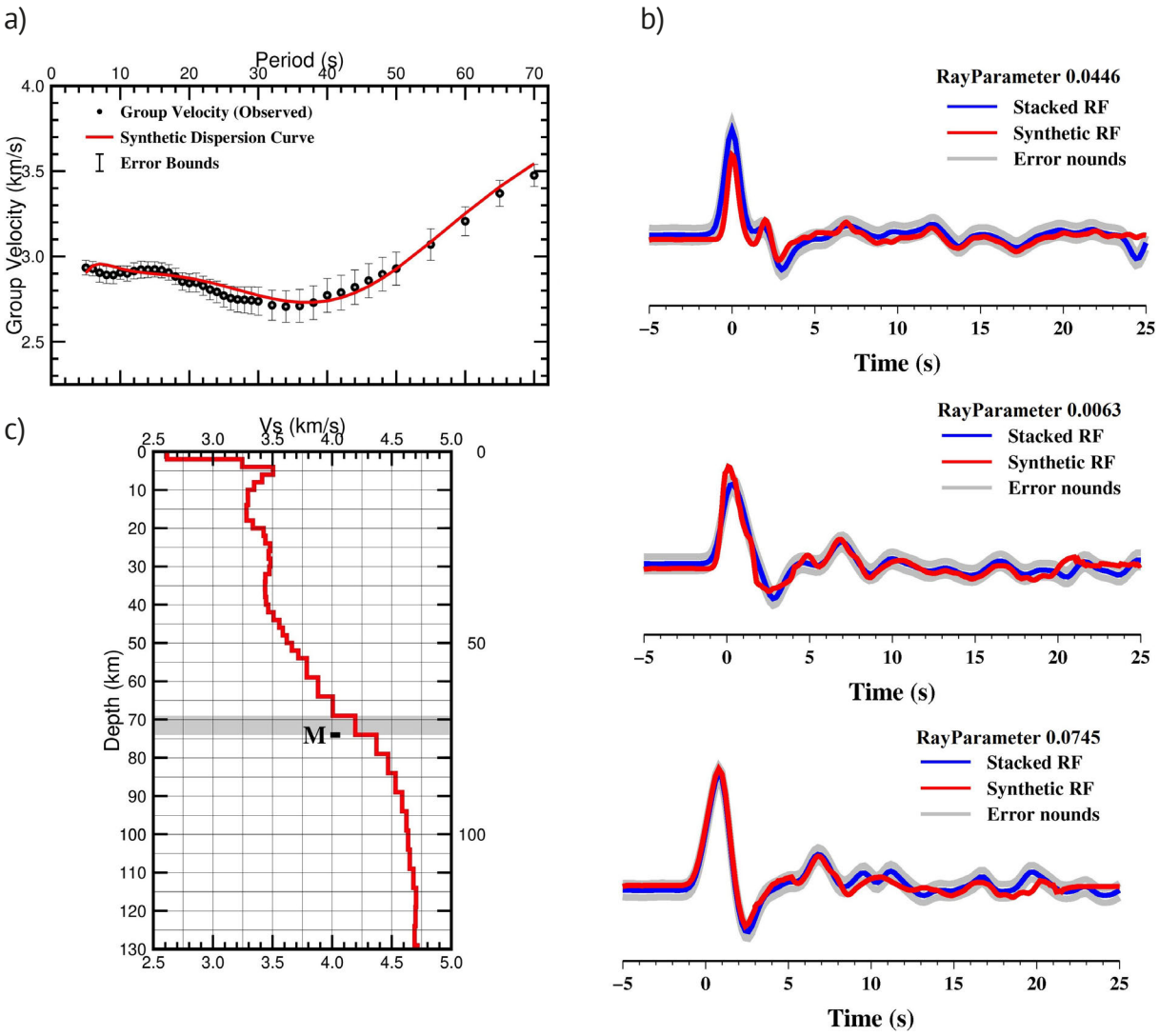

Figure 4. The results obtained from the joint inversion for a selected location at 81.5°N and 32°E. (a) Observed group velocities (black circles) fitted to dispersion curve (red line) with error bars. (b) Fitting of the stacked receiver functions (blueline) with synthetic receiver functions (red line) for different ray parameter and error bounds (grey lines). (c) Final inverted shear wave velocity model, where M denotes the Moho depth and grey shaded region denotes the layer with shear velocity >4.0 km/s.

The standard error of the RFs is the error that generated while constructing the interpolated receiver functions. It is calculated from the standard deviation of the waveforms in the bin where the interpolated RF has been constructed from a weighted stack average of all the waveforms within the particular distance range. The standard error of the surface wave dispersion data is the maximum error that generated while performing the tomographic inversion. In the tomography, the traveltimes of the surface wave are converted to group velocities by applying a set of operators to the traveltime and amplitude fields. In this process, the random error of the traveltime produces scattering in the group velocity measurements obtained after performing the tomography. We perform the tomography at each grid point by considering the random errors in the traveltime and takingthe standard deviation of the group velocities produced at each grid. Figure 4 shows the fitting of the surface wave dispersions and the RF forall the three bins. This provides us with a more reliable result to accept for our study.

3.5 Depth Resolution

The Rayleigh wave group velocities are measured for different frequencies, which are sensitive to different depths inside the Earth. For a layered Earth model, the relationship between the Rayleigh wave group velocity

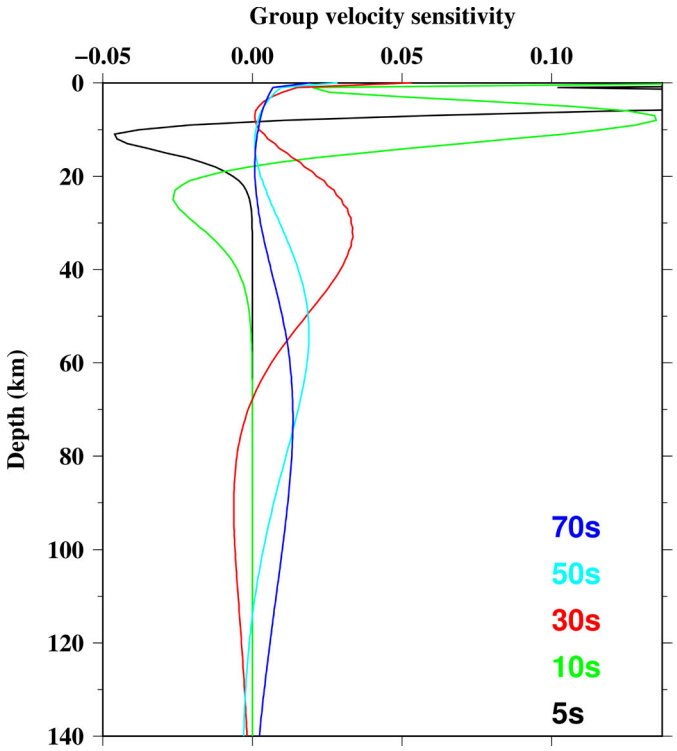

Figure 5. Sensitivity kernels plot for the fundamental mode Rayleigh wave group velocities at 5, 10, 30, 50 and 70 s periods with respect to the corresponding depth.

measurements at different frequencies to the different depth inside the Earth can be illustrated using sensitivity kernels. Figure 5 presents a sensitivity kernel that shows the sensitivity of the Rayleigh wave group velocity to the shear velocity perturbations at increasing depths. We have shown the depth dependence of the velocity sensitivity kernels at 5, 10, 30, 50 and 70 s periods. These sensitivity kernelswere constructed using the programGrv_Sens_ Kernel. The depth sensitivity increases with increasing time periods. Figure 5 demonstrates that the 5 s period is sensitive to depths ranging from 5 to 10 km, as the time period increases, the depth sensitivity increases to approximately 130 km for the of 70 s period. The sensitivity kernel becomes more flat with increasing time periods, indicating a larger depth averaging. Therefore, we could able to map down to a depth of 130 km beneath western Tibet from this study.

3.6 Uncertainty estimation

Estimating uncertainty is one of the crucial parts in modelling the structure from any seismological data. For both the datasets, RFs and the surface wave dispersion, the error bars are computed while generating the data. We only considered measurements with acceptable error bars. We used the bootstrap method [Efron and Tibshirani, 1986] to estimate the uncertainties in computing the velocities and the Moho depth. For each set of RFs, the samples were created by choosing the RFs randomly with repetition. A total of 25 bootstrap samples were created for the study. We performed interpolation (described in section 3.1) for all these sets of sample and then performed the joint inversion. The maximum variation of approximately ± 3 km for the Moho depth was observed, whole for shear wave velocity, a maximum variation of approximately ± 0.07 km/s was observed.

4. Results

We utilized a joint inversion technique, combining the interpolated RF and the Rayleigh wave group velocity dispersion, to construct a 3D model of shear wave velocity for western Tibet region. The resulting shear wave velocity

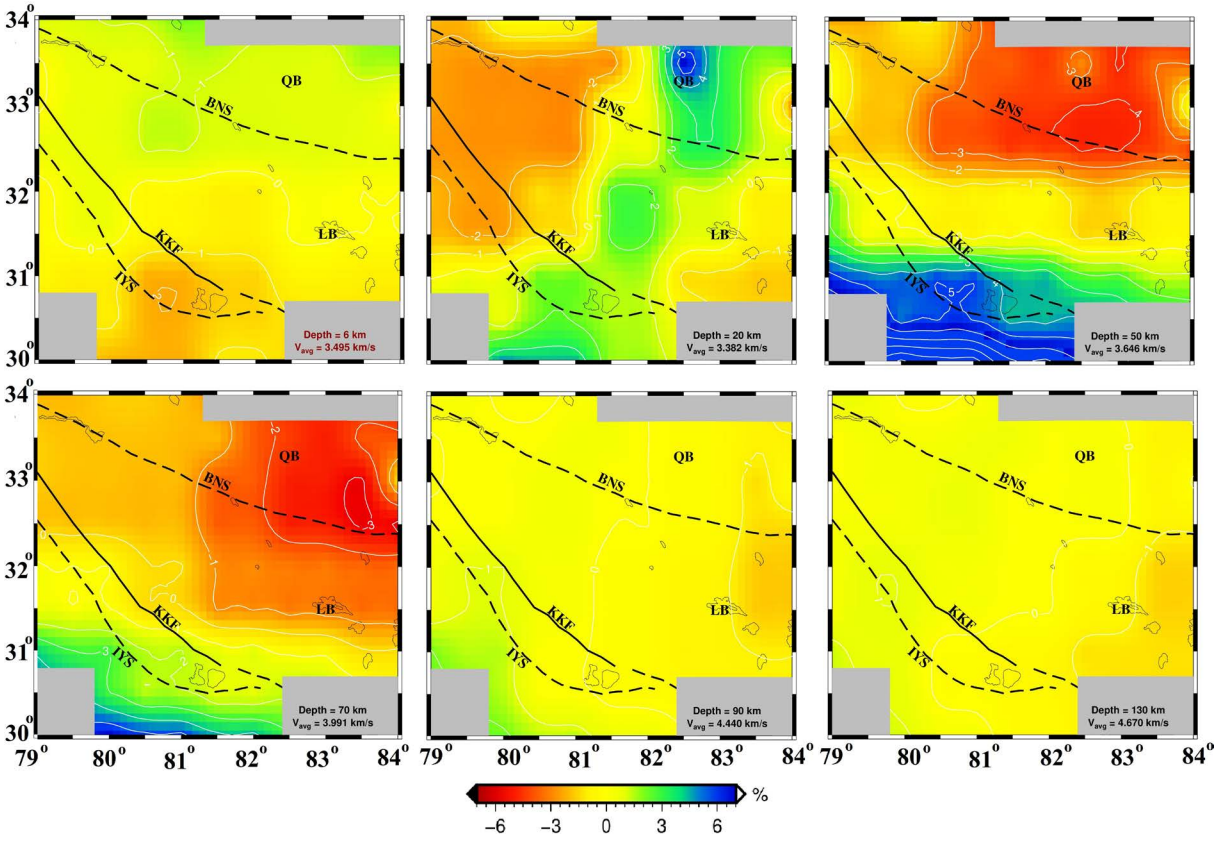

Figure 6. Shear wave velocity perturbation at different depth ranges, 6 km, 20 km, 50 km, 70 km, 90 km and 130 km. The velocity perturbations are plotted relative to the average shear velocity of the respective depths. The average shear velocity is written on the bottom left corner of each plot.

model at coordinates 81.5N and 32E is depicted in Fig. 4. In Fig.4a, we present the comparison between the inverted dispersion (red line) and the observed dispersion (black circles) with error bars. Figure 4b showcases the fitting of the receiver functions, both observed and synthetic, accompanied by error bars. Finally, Figure 4c displays the comprehensive shear wave velocity model obtained through all stages of the joint inversion process, with the Moho

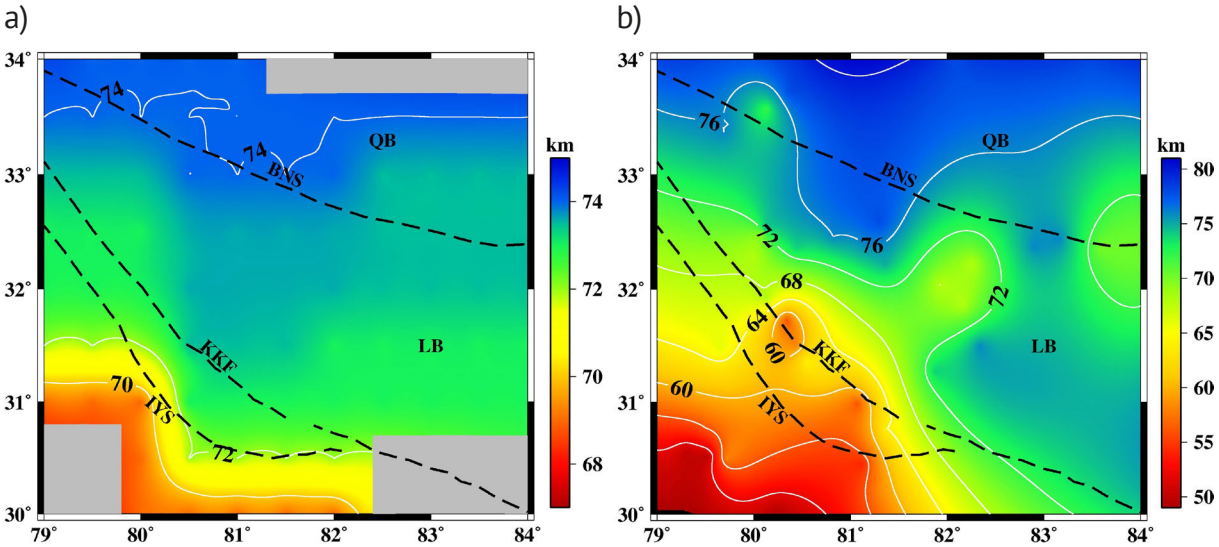

Figure 7. The estimated Moho depth beneath western Tibet from the (a) present study and the research by (b) Gilligan et al. [2015]. Additionally, significant geological features and faults/shear zones are also shown.

depth indicated by an arrow. The gray shaded area in the figure corresponds to a high velocity layer, characterized by shear wave velocities exceeding 4.0 km/s.

To gain a better understanding of how velocity anomalies vary with depth, we have depicted the three-dimensional (3D) shear wave velocity variations that achieved through the joint inversion as horizontal slices at varying depths beneath western Tibet. Figure 6 showcases velocity slices at depths of 6, 20, 50, 70, 90, and 130 km, illustrating the deviations in velocity relative to the average shear wave velocity. The average velocity is determined by taking the arithmetic mean of shear velocities at each point within that particular depth. Then we try to understand the layer wise crustal structure based on velocity variations. In general, the crust can be categorized

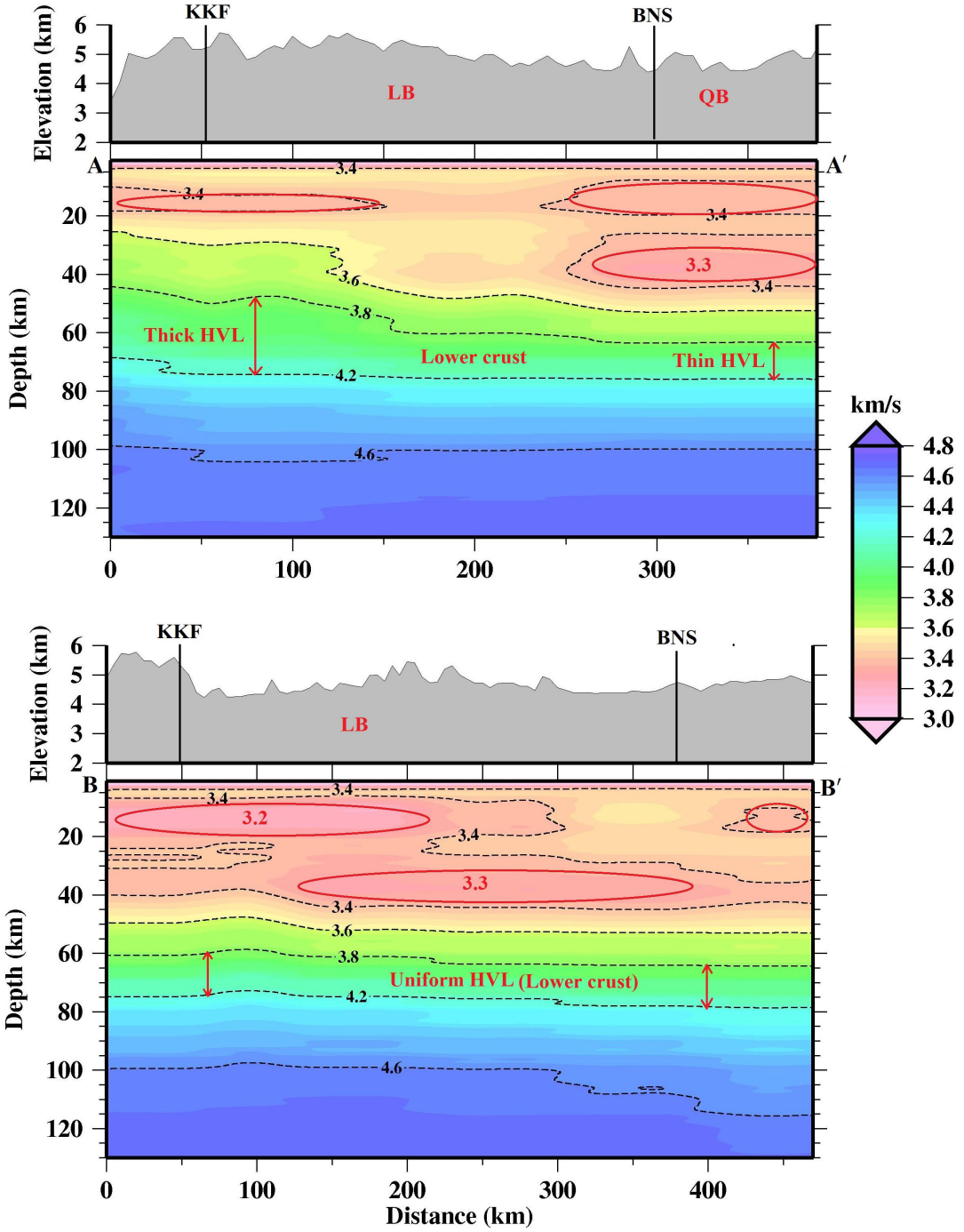

Figure 8. Absolute shear wave velocity variation in the vertical cross-sections along the two profiles AA′ and BB′ (shown in figure 1b). Main features are marked by red ellipse. The topography of the region is plotted on the top. The red dashed lines represent the location of tectonic boundary and shear zones.

into upper, middle, and lower layers based on distinct shear wave velocities. The upper crust exhibits shear wave velocities below 3.5 km/s, while the middle crust ranges between 3.5 km/s and 3.8 km/s. The lower crust possesses shear velocities greater than 3.8 km/s [Christensen and Mooney, 1995; Christensen 1996].

In western Tibet, we observe the upper crustal velocity down to a depth of 4 km and the mid-crustal velocity down to around 54 km depth. We observe a comparatively slow shear wave velocity anomaly extending from around 8 km to approximately 40 km depth (less than and equal to 3.4 km/s). The largest velocity gradient, where the shear wave velocity exceeds 4.2 km/s, is considered the Moho boundary beneath the region. We ensure that this depth is consistent with the delay time of the P-to-s conversion of the RFs. Experimental studies on rocks and minerals in the continental crust have identified the Moho as the sharp gradient zone where shear wave velocity shows a pronounced variation [Christensen and Mooney, 1995; Christensen, 1996]. The lateral variation of the Moho depth in our study region is shown in Figure 7a.

Inmost parts of western Tibet, the Moho depth is observed around 74 km, except in the south of the IYS. From the IYS to the south of the region, the Moho depth is estimated to range from 65 km to 72 km. In the northern part of western Tibet, we observe a comparatively slow velocity anomaly at depths of between 40 and 65 km. In the shallow mantle of western Tibet (as deep as 130 km), the velocities have been found to increase with depth. The shear wave velocity varies from 4.4 km/s to 4.7 km/s in the shallow upper mantle of western Tibet. The absolute shear wave velocity variations along the N-S and E-W striking vertical cross section profiles, AA′ and BB′, respectively are shown in Figure 8. Both the profiles traverse through all the shear zones (BNS, KKF and IYS) in the region. At depths of around 8 km to 40 km, both profiles clearly illustrate the mid crustal slow velocity anomaly. The right hand side of the AA′ profile exhibits a gradual decrease in velocity between depths of 40 km and 60 km (~3.6-3.7 km/s). This anomaly is most likely associated with the northern part of western Tibet. The average shear velocity model for the study region, depicted in Figure 9, reveals the estimated shear wave velocities at various depths beneath western Tibet. On average, the upper crust exhibits a shear wave velocity of approximately 2.6 km/s, while the middle crust shows a velocity of around 3.5 km/s. Deeper in the lower crust, the velocity increases to about 3.9 km/s, and in the shallow upper mantle, it reaches approximately 4.5 km/s. These values provide an overall representation of the average shear wave velocities in the specific region.

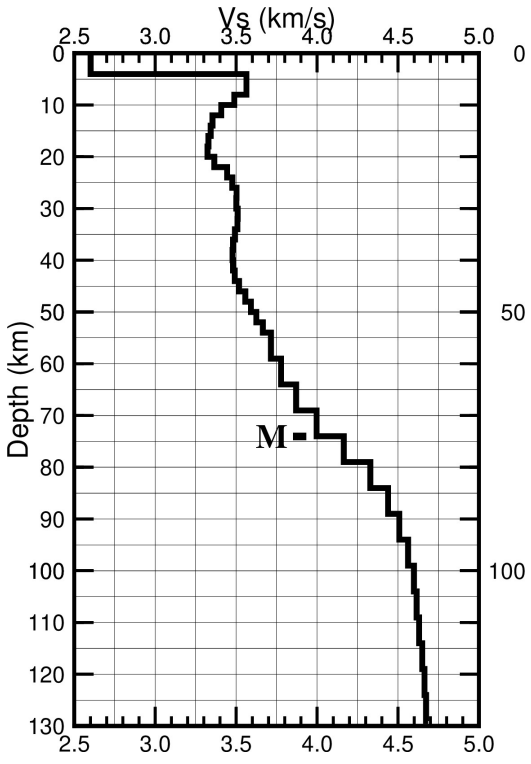

Figure 9. The average shear wave velocity model for the Western Tibet, where M in the plot is the average Moho depth beneath the western Tibet.

5. Discussions

5.1 Nature of the Moho

The estimated Moho depth from our present study suggests thatit isgradually increasing from south to north beneath western Tibet. From the observed velocity models, we noticed that the overall progression from the crust to the mantle appeared to be gradational. Overall, our results indicate that the estimated Moho depth of Tibetan block is thicker than the Himalayan block (Fig. 7a). Based on the Hi-CLIMB experiment, Nabelek et al. [2009] suggested that such type of Moho geometry is present because of Indian lithosphere intruding underneath the southern half of the LB. It is interesting to notice that Owens and Zandt [1997] also interpreted their results in the same manner as the intrusion of Indian lithosphere far northward up to the BNS. For such type of models, the Moho geometry could be easily explained by the under-thrusting of Indian plate beneath Tibetan plateau.

Our estimated Moho depth variation for the southernmost part of the study region (South of KKF) lies in between 65 and 70 km. Here, the Moho depths are 6-8 km shallower than those estimated by Gilligan et al. [2015]. With minor variations in depth, our results showed that the average Moho depth is around 74 km under the LB and QB. Within the LB, our calculated Moho depth is in good agreement with the previous RF and tomography studies [Wittlinger et al., 2004; Zhang et al., 2014; Gilligan et al., 2015; Razi et al., 2016]. Based on the analysis of travel time tomography by Razi et al. [2014], they observed a significant change in the body wave velocity between 70 and 80 km, which they interpreted as the Moho depth. By using Common Conversion Point (CCP) stacks of RFs, Zhang et al. [2014] noticed the Moho at 67-77 km depth, while Wittlinger et al. (2004) observed at a depth of 70-78 km. In a joint inversion approach (RF and surface wave), Gilligan et al. [2015] observed a variation in Moho depth between 68 and 78 km beneath the LB.

However, our estimated Moho depth is shallower (~74 km) than the depth of 84-90 km observed by Wittlinger et al. [2004] beneath the QB. But it is consistent with a few other studies [Zhang et al., 2014; Gilligan et al., 2015; Razi et al., 2016]. Previous studies have noted an important feature related to the geometry of Moho (Moho offset) in the study region. It has been suggested that Moho has a ~12 km offset at the BNS and ~5-10 km at the KKF [Wittlinger et al. 2004; Zhang et al., 2014]. However, we find gradual changes in the Moho in these locations instead of a Moho offset which is compatible with the finding of Gilligan et al. [2015]. Overall, although a few locations of study region show the Moho depth differences of 3-4 km compared to previous studies, these differences fall within the acceptable error limit. Discrepancies between the estimates of Moho depth from different studies may exist due to differences in the underlying methods and the resolution of data. Additionally, it also depends on where the Moho is picked in the velocity models and how much velocity contrast at the crust mantle boundary. Because of these factors, it is also a matter of individual interpretation, which can lead to differences in results.

In several parts of Himalaya region, many studies support partial eclogitization in the lower crust. For example, (i) the RF study by Zhang et al. [2014]; (ii) joint inversion studies by Giligan et al. [2015] and, (iii) the tomographic studies by Razi et al. [2016]. The gradational Moho observed in the present study also potentially supports lower crustal eclogitization. The comparatively low amplitude and broad P-to-s (Ps) phases of the RFs suggest the gradational nature of the Moho observed in the joint inversion models. Since eclogitization is a progressive process governed by the availability of hydrous melt, the systematic change in RF signature might be explained by lower crustal eclogitiation [Hetenyi et al., 2007].

However, several other studies have observed steps in the Moho beneath Tibetan plateau. For example, Hirn et al. [1984], observed a step in the Moho at IYS, Wittilinger et al. (2004] observed a Moho step at BNS, and Zhang et al. [2014] observed a Moho step at Ghoza fault etc. Our results do not observe any such type of Moho step at these locations, which is consistent with the previous study by Gilligan et al. [2015]. The Moho step reported by Wittilinger et al. [2004] and Zhang et al. [2014] is based on the analysis of Depth migration results. Gilligan et al., [2015] suggested that sometimes CCP stacks can produce artifact feature and therefore the reported Moho step in the study region may be incorrect.

5.2 Mid crustal slow velocity

In general, for a normal continental crust, the shear wave velocity ranges fall between 3.5 and 3.8 km/s for mid crust [Christensen, 1996]. We observed a quite slow shear wave velocity anomaly (Vs 3.0-3.4 km/s) at the mid crustal

depth of the study region, starting from ~8 km and extending down to ~40 km depth. During our examination of the mid-crustal slow velocity structure, we encountered two intriguing characteristics (Fig. 8). They are (i) First, even though we find such a type of structure (mid-crustal slow velocity layer), this signature is not uniform and present everywhere; (ii) Second, it is dominant beneath the north-eastern part of the study region. Various geophysical and geological investigations have noticed two different types of observations regarding the mid crustal slow velocity layer across different parts of Himalaya and Tibetregion [Rapine et al., 2003; Caldwell et al., 2009; Rai et al., 2006; Oreshin et al., 2008; Razi et al., 2014; Gilligan et al., 2015; Bao et al., 2015]. Some studies find a slow velocity anomaly [Rapine et al., 2003; Caldwell et al., 2009; Gilligan et al., 2015; Bao et al., 2015) at the mid crustal depth, while others do not find such type of signature [Rai et al., 2006; Oreshin et al., 2008; Razi et al., 2014].

Caldwell et al. [2009] observed a slow mid-crustal velocity beneath the north-west Himalaya, which is just on the western margin of the present study. They suggested that this type of structure cannot be explained merely by any dry metamorphic or plutonic rocks. The partial melting in the presence of water in the upper crust would produce such slow velocity layer according to Caldwell et al. [2009]. Giligan et al. [2015] also noticed a similar mid-crustal slow velocity anomaly beneath western Tibet. A mid-crustal slow velocity has also been observed to the east of the present study by several authors [Bao et al., 2015; Cotte et al., 1999; Rapine et al., 2003]. They have interpreted the slow velocity anomaly with the presence of melt as a result of water saturation and strong heat production in the crust, which occurs due to thickening of the crust in the region [Bao et al., 2015; Cotte et al., 1999; Rapine et al., 2003]. On the other hand from body wave tomography models, Razi et al. [2014] did not observe any such type of mid-crustal slow velocity anomaly beneath western Tibet. Instead, they observe a well-defined boundary for south and north of the KKF. Unfortunately, we do not observe any significant boundary in the south and north of KKF in the present study. Few other studies also do not observe any well-defined boundary to the north and south of the KKF [Giligan et al., 2015]. The observed mid crustal slow velocity beneath the entire western Tibet crust is suggestive of the fact that the KKF does not separate the crust of the Himalaya and the Tibet.

A few questions are of utmost importance before interpreting the results, such as the reliability and resolution of the observed seismic images. It has been proven that individual data cannot resolve certain Earth features due to their own limitations and sensitivity issues. In contrast, combining multiple data sets (receiver function and surface wave) during inversion can help to reduce ambiguity and produce a more accurate image. Gilligan et al. [2015] pointed out that few previous studies had not been able to resolve slow velocity layers because theyused a single data set during inversion (either receiver function or dispersion data). In the present study, we used a joint inversion approach, so the reliability and resolution of the structure are acceptable. Furthermore, we carried out forward modelling to assess the reliability of slow velocity layers and noticed that the inclusion of slow velocity layers in the velocity models did not affect the fit between the observed and synthetic data sets. Figure S8 shows the fitting of the RFs and dispersions along with the model from the forward modelling.

The observed signature of mid-crustal slow velocity cannot be simply described by the presence of general solid dry crustal rocks. Christensen [1996] provides the laboratory experimental values of the velocity of metamorphic rocks at room temperature and lithostatic pressure at certain depths. For the mid-crustal temperature, the velocity can be reduced by 0.2 m/s/°C [Kern et al., 2001]. In general, the mid-crustal temperature in the Himalaya and Tibet can be considered as ~600 °C [Jamieson et al., 2004; Craig et al., 2012]. Therefore, at a gradient of 0.2 m/s/°C, these temperatures are not sufficient to bring the room temperature laboratory calculated velocity to the one that we observed in our study. Thus, we believe that the observed mid-crustal slow velocity anomaly cannot be merely explained by any dry metamorphic or plutonic rocks.

In general, the slow velocity can also be explained by elevated temperatures [Christensen, 1979]. According to McKenzie and Priestley [2008], the process of radioactivity in thickened crusts would increase the temperature of the middle crust. As a consequence, the shear wave velocity would decrease. Another plausible explanation of the slow velocity is the presence of partial melts. Several studies have concluded that the low resistivity anomalies revealed from magnetotelluric imaging in north-west Himalaya and the Tibet can be explained by these partial melts [Arora et al., 2007; Unsworth et al., 2005]. Our observed slow velocity anomaly shows a good spatial correspondence in depth with slow resistivity anomaly of Arora et al. [2007]. Usually, partial melts or hydrous fluids, or both, can easily lower the velocity by 7-17%, resulting in a slow velocity in the structure [Watanabe, 1993; Takei, 2000). These are the plausible explanations given for the high-reflectivity, slow-velocity, or low-resistivity geophysical anomalies beneath Tibet and the Himalaya [Caldwell et al., 2009; Makovsky and Kemplerer, 1999; Li et al., 2003; Unsworth et al., 2005; Nelson et al., 1996]. The channel flow model under the Tibet and Himalaya has already been argued by some studies, but we do not find a stronger argument for it using our current dataset along with the obtained results.

5.3 Nature of lower crust and shallow upper mantle

Several important features can be observed in the shear wave velocity images presented in this study. These include: (i) First, the observed velocity variation is significantly different from south to the north at the deeper crustal depth, (ii) Second, the velocity anomalies along profile AA′ clearly show a dipping structure from the Himalaya to Tibetan Plateau, whereas this feature is less evident along BB′ profile, and (iii) Third, the thickness of high-velocity layer (3.8-4.2 km/s) also changes with location.

We observe a comparatively slow velocity anomaly (3.2-3.6 km/s) in the lower crust (40-60 km depth; profile AA′) of western Tibet, which starts from the northernmost part of the LB and continues up to Qiantang block. However, the southern part of our study region, does not exhibit the same type of slow velocity anomaly at those depth, but rather a relatively high velocity zone (3.8-4.2 km/s) (Fig. 6). The boundary related to thick high velocity layer (3.8-4.2 km/s) above the Moho can be seen from the southernmost part of the study region to the south of the LB, and beyond that the layer looks comparatively thinner. We interpret that the presence of the high velocity zone in the lower crust may be related to eclogite being transformed from the mafic lower crust. Razi et al. [2014] also observed a high velocity anomaly in the lower crust and upper-most mantle and proposed similar interpretation. This entire process would require the Indian crust to underthrust beneath Tibetan plateau.

In the Earth science community, identifying the northern limit of the Indian lithosphere beneath Tibet is of primary interest. Although several studies have been conducted, it remains one of the most challenging and controversial topics. Studies generally define the northern limit of the Indian lithosphere based on evidence such as fast velocities [Huang et al., 2009] and converting boundaries [Nabelek et al., 2009; Schulte-Pelkum et al., 2005]. Using data from the Hi-CLIMB project, Nabelek et al. [2009] observed a sharp difference in the seismic characteristics of the lower crust and uppermost mantle south of the LB and the north of it, extending up to BNS. They interpreted the zone north of 31°N and south of BNS as the boundary between the Indian and Eurasian plates. Our study region lies just adjacent to the seismic profile of the Hi-CLIMB project in the western part. It is also possible that the velocity variation observed in our study is indicative of the northern limit of the Indian lithosphere. However, here we cannot interpret the northern boundary to be the BNS, like the interpretation by Nabeleket al. [2009], as we observe a similar feature beyond BNS in our study region. Some studies [Priestley et al., 2006; Zhao et al., 2010] on the lithosphere of the Himalaya and Tibet states that the underthrusting process of the Indian plate northward beneath the Eurasian plate extends up to the northernmost boundary of Tibetan plateau. Razi et al. [2016] performed upper mantle tomographic studies in the same study region of ours using regional and teleseismic arrival times of compressional and shear wave. Their study clearly shows that the colder material underneath the Himalaya and the southern part of Tibetan plateau is limited only up to the LB.

6. Conclusions

We have successfully determined the shear wave velocity variation of the crust and shallow upper mantle structureof western Tibet. The new geophysical technique, especially the interpolated technique of the receiver function, has proven effective at overcoming the poorly sampled back azimuthal fluctuations. By combining two data sets using ambient noise and the earthquakes, we have obtained a wide range of surface wave dispersions, ranging from 5 s to 70 s. And finally, the joint inversion of receiver function and the surface wave dispersions gives us a significant insight of the structure beneath western Himalaya and Tibet with best possible resolution using the existing dataset. The Moho depth in the northern part of western Tibet is ~74 km and in the southern part is ~69 km. The observed gradational change in the Moho is indicative of the lower crustal eclogitazation. The presence of partial melts is likely responsible for the thick mid-crustal slow velocity beneath western Tibet. In the south and north of the LB, there is a significant change in the lower crustal velocity, which we interpret as the manifestation of the Indian lithosphere extending to the southern part of the block.

Acknowledgement. The dataset (which is open to all) used for the study are provided by the IRIS DMC. We have processed the data using Seismic Analysis Code (SAC) and figures are plotted using Generic Mapping Tools (GMT) [Wessel and Smith, 1998]. The joint inversion has been performed using the computer programs in seismology by Robert Herrmann (http://www.eas.slu.edu/eqc/eqc_cps/CPS/CPS330.html). RD and US acknowledge the Ramanujan fellowship research grant support from the SERB-DST.

References

Allégre, C.O., V. Courtillot, P. Tapponnier, A. Hirn, M. Mattauer, C. Coulon, J.J. Jaeger, J. Achache, U. Schärer, J. Marcoux and J.P. Burg (1984). Structure and evolution of the Himalaya-Tibet orogenic belt, Nature, 307, 17-22.

Argand, E. (1924). Le tectonique de l'Asie, Proceedings of the 13th International Geological Congress, 7, 171-372.

Arora, B.R., M.J. Unsworth and G. Rawat (2007). Deep resistivity structure of the northwest Indian Himalaya and its tectonic implications, Geophys. Res. Lett., 34, L04307.

Avouac, J.-P. and P. Tapponnier (1993). Kinematic model of active deformation in central Asia, Geophys. Res. Lett., 20, 895-898.

Bao, X., X. Song and J. Li (2015). High-resolution lithospheric structure beneath Mainland China from ambient noise and earthquake surface-wave tomography, Earth Planet. Sci. Lett., 417, 132-141.

Barmin, M.P., M.H. Ritzwoller and A.L. Levshin (2001). A Fast and Reliable Method for Surface Wave Tomography, Pure Appl.Geophys., 158, no. 8, 1351-1375.

Basuyau, C., M. Diament, C. Tiberi, G. Hetényi, J. Vergne and A. Peyrefitte (2013). Joint inversion of teleseismic and GOCE gravity data: application to the Himalayas, Geophys. J. Int., 193, 149-160.

Beaumont, C., R.A. Jamieson, M.H. Nguyen and B. Lee (2001). Himalayan tectonics explained by extrusion of a low-viscosity crustal channel coupled to focus surface denudation, Nature, 414, 738-742.

Bensen, G.D., M.H. Ritzwoller, M.P. Barmin, A.L. Levshin, F. Lin, M.P. Moschetti, N.M. Shapiro and Y. Yang (2007). Processing seismic ambient noise data to obtain reliable broad-band surface wave dispersion measurements, Geophys. J. Int., 169, 1239-1260.

Bhattacharya, S.N. (1983). Higher order accuracy in multiple filter technique, B. Seismol. Soc. Am., 73, 1395-1406.

Bilham, R. (2004). Earthquakes in India and the Himalaya: tectonics, geodesy and history, Ann. Geophys., 47, 839-858

Caldwell, W.B., S.L. Klemperer, S.S. Rai and J.F. Lawrence (2009). Partial melt in the upper-middle crust of the northwest Himalaya revealed by Rayleigh wave dispersion, Tectonophysics, 477, 58-65.

Chai, C., C.J. Ammon, M. Maceira and R.B. Herrmann (2015). Inverting interpolated receiver functions with surface wave dispersion and gravity: Application to the western U.S. and adjacent Canada and Mexico, Geophys. Res. Lett., 42, 4359-4366.

Christensen, N.I. (1979). Compressional wave velocities in rocks at high temperatures and pressures, critical thermal gradients, and crustal low-velocity zones, J.Geophys. Res. Solid Earth, 84, 6849-6857.

Christensen, N.I. (1996). Poisson's ratio and crustal seismology, J. Geophys. Res. Solid Earth, 101, 3139-3156.

Christensen, N.I. and W.D. Mooney (1995). Seismic velocity structure and composition of the continental crust: A global view, J. Geophys. Res. Solid Earth, 100, 9761-9788.

Copley, A. and D. McKenzie (2007). Models of crustal flow in the India-Asia collision zone, Geophys. J. Int., 169, 683-698.

Cotte, N., H. Pedersen, M. Campillo, J. Mars, J.F. Ni, R. Kind, E. Sandvol and W. Zhao (1999). Determination of the crustal structure in southern Tibet by dispersion and amplitude analysis of Rayleigh waves, Geophys. J. Int., 138, 809-819.

Craig, T.J., A. Copley and J. Jackson (2012). Thermal and tectonic consequences of India underthrusting Tibet, Earth Planet. Sci. Lett., 353-354, 231-239.

Dziewonski, A., S. Bloch and M. Landisman (1969). A technique for the analysis of transient seismic signals, B. Seismol. Soc. Am., 59, 427-444.

Efron, B. and R. Tibshirani (1986). Bootstrap Methods for Standard Errors, Confidence Intervals, and Other Measures of Statistical Accuracy, Statistical Science, 1, 54-75

England, P. and G. Houseman (1986). Finite strain calculations of continental deformation: 2. Comparison with the India-Asia Collision Zone, J. Geophys. Res. Solid Earth, 91, 3664-3676.

England, P. and G. Houseman (1985). Role of lithospheric strength heterogeneities in the tectonics of Tibet and neighbouring regions, Nature, 315, 297-301.

England, P. and D. McKenzie (1982). A thin viscous sheet model for continental deformation, Geophys. J. Int., 70, 295-321.

England, P. and D. McKenzie (1983). Correction to: a thin viscous sheet model for continental deformation, Geophys. J. Int., 73, 523-532.

Gilligan, A., K.F. Priestley, S.W. Roecker, V. Levin and S.S. Rai (2015). The crustal structure of the western Himalayas and Tibet, J.Geophys. Res. Solid Earth, 120, 3946-3964.

Godin, L., D. Grujic, R.D. Law and M.P. Searle (2006). Channel flow, ductile extrusion and exhumation in continental collision zones: an introduction, Geological Society, London, Special Publications, 268, 1-23.

Green, O.R., M.P. Searle, R.I. Corfield and R.M. Corfield (2008). Cretaceous-Tertiary Carbonate Platform Evolution and the Age of the India-Asia Collision along the Ladakh Himalaya (Northwest India), J. Geol., 116, 331-353.

Griffin, J.D., R.L. Nowack, W.-P. Chen and T.-L. Tseng (2011). Velocity Structure of the Tibetan Lithosphere: Constraints from P-Wave Travel Times of Regional Earthquakes, B. Seismol. Soc. Am., 101, 1938-1947.

Grujic, D., L.S. Hollister and R.R. Parrish (2002). Himalayan metamorphic sequence as an orogenic channel: insight from Bhutan, Earth Planet Sci Lett, 198, 177-191.

Herrmann, R.B. (1973). Some aspects of band-pass filtering of surface waves, B. Seismol. Soc. Am., 63, 663-671.

Herrmann, R.B. and C.J. Ammon (2004). Surface Waves, Receiver Functions and Crustal Structure. Computer Programs in Seismology, Version 3.30. Saint Louis University.

Hetényi, G., R. Cattin, F. Brunet, L. Bollinger, J. Vergne, J.L. Nábělek and M. Diament (2007). Density distribution of the India plate beneath the Tibetan plateau: Geophysical and petrological constraints on the kinetics of lower-crustal eclogitization, Earth. Planet. Sci. Lett., 264, 226-244.

Hirn, A. et al. (1984). Crustal structure and variability of the Himalayan border of Tibet, Nature, 307, 23-25.

Huang, G.-C.D., F.T. Wu, S.W. Roecker and A.F. Sheehan (2009). Lithospheric structure of the central Himalaya from 3-D tomographic imaging, Tectonophysics, 475, 524-543.

Jamieson, R.A., C. Beaumont, S. Medvedev and M.H. Nguyen (2004). Crustal channel flows: 2. Numerical models with implications for metamorphism in the Himalayan-Tibetan orogen, J. Geophys. Res. Solid Earth, 109.

Julià, J., C.J. Ammon, R.B. Herrmann and A.M. Correig (2000). Joint inversion of receiver function and surface wave dispersion observations, Geophys. J. Int., 143, 99-112.

Kern, H., T. Popp, F. Gorbatsevich, A. Zharikov, K.V. Lobanov and Yu. P. Smirnov (2001). Pressure and temperature dependence of VP and VS in rocks from the superdeep well and from surface analogues at Kola and the nature of velocity anisotropy, Tectonophysics, 338, 113-134.

Kosarev, G., R. Kind, S.V. Sobolev, X. Yuan, W. Hanka and S. Oreshin (1999). Seismic Evidence for a Detached Indian Lithospheric Mantle beneath Tibet, Science (1979), 283, 1306-1309.

Law, R.D., M.P. Searle and R.L. Simpson (2004). Strain, deformation temperatures and vorticity of flow at the top of the Greater Himalayan Slab, Everest Massif, Tibet, J. Geol. Soc. London, 161, 305-320.

Law, R.D., M.P. Searle and L. Godin (2006). Channel Flow, Ductile Extrusion and Exhumation in Continental Collision Zones. Geological Society, London, Special Publications, 268.

Li, C., R.D. van der Hilst, A.S. Meltzer and E.R. Engdahl (2008). Subduction of the Indian lithosphere beneath the Tibetan Plateau and Burma, Earth Planet Sci Lett, 274, 157-168.

Li, S., M.J. Unsworth, J.R. Booker, W. Wei, H. Tan and A.G. Jones (2003). Partial melt or aqueous fluid in the mid-crust of Southern Tibet? Constraints from INDEPTH magnetotelluric data, Geophys. J. Int., 153, 289-304.

Ligorría, J.P. and C.J. Ammon (1999). Iterative deconvolution and receiver-function estimation, Bulletin of the Seismological Society of America, 89, 1395-1400.

Lin, F.-C., M.P. Moschetti and M.H. Ritzwoller (2008). Surface wave tomography of the western United States from ambient seismic noise: Rayleigh and Love wave phase velocity maps, Geophys. J. Int., 173, 281-298.

Makovsky, Y. and S.L. Klemperer (1999). Measuring the seismic properties of Tibetan bright spots: Evidence for free aqueous fluids in the Tibetan middle crust, J.Geophys. Res. Solid Earth, 104, 10795-10825.

Matte, P. (1996). Tectonics of Western Tibet, between the Tarim and the Indus, Earth Planet Sci. Lett., 142, 311-330.

MKenzie, D. and K. Priestley, 2008, The influence of lithospheric thickness variations on continental evolution, Lithos, 102, nos. 1-2, 1-11, doi: 10.1016/j.lithos.2007.05.005.

Molnar, P. and P. Tapponnier (1975). Cenozoic Tectonics of Asia: Effects of a Continental Collision: Features of recent continental tectonics in Asia can be interpreted as results of the India-Eurasia collision, Science (1979), 189, 419-426.

Murphy, M.A., A. Yin, P. Kapp, T.M. Harrison, D. Lin and G. Jinghui (2000), Southward propagation of the Karakoram fault system, southwest Tibet: Timing and magnitude of slip, Geology, 28, 451.

Nábělek, J., G. Hetényi, J. Vergne, S. Sapkota, B. Kafle, M. Jiang, H. Su, J. Chen, B.-S. Huang and the H.-C. Team (2009). Underplating in the Himalaya-Tibet Collision Zone Revealed by the Hi-CLIMB Experiment, Science (1979), 325, 1371-1374.

Nelson, K.D. et al. (1996). Partially Molten Middle Crust beneath Southern Tibet: Synthesis of Project INDEPTH Results, Science (1979), 274, 1684-1688.

Ni, J. and M. Barazangi (1984). Seismotectonics of the Himalayan Collision Zone: Geometry of the underthrusting Indian Plate beneath the Himalaya, J.Geophys. Res. Solid Earth, 89, 1147-1163.

Oreshin, S., S. Kiselev, L. Vinnik, K. Surya Prakasam, S.S. Rai, L. Makeyeva and Y. Savvin (2008). Crust and mantle beneath western Himalaya, Ladakh and western Tibet from integrated seismic data, Earth. Planet. Sci. Lett., 271, 75-87.

Owens, T.J. and G. Zandt (1997). Implications of crustal property variations for models of Tibetan plateau evolution, Nature, 387, 37-43.

Priestley, K., E. Debayle, D. McKenzie and S. Pilidou (2006). Upper mantle structure of eastern Asia from multimode surface waveform tomography, J.Geophys. Res., 111, B10304.

Rai, S.S., K. Priestley, V.K. Gaur, S. Mitra, M.P. Singh and M. Searle (2006). Configuration of the Indian Moho beneath the NW Himalaya and Ladakh, Geophys. Res. Lett., 33, L15308.

Rapine, R., F. Tilmann, M. West, J. Ni and A. Rodgers (2003). Crustal structure of northern and southern Tibet from surface wave dispersion analysis, J.Geophys. Res. Solid Earth, 108.

Rawlinson, N. and W. Spakman (2016). On the use of sensitivity tests in seismic tomography, Geophys. J. Int., 205, 1221-1243.

Razi, A.S., V. Levin, S.W. Roecker and G.D. Huang (2014). Crustal and uppermost mantle structure beneath western Tibet using seismic traveltime tomography, Geochem.Geophys.Geosys., 15, 434-452.

Razi, A.S., S.W. Roecker and V. Levin (2016). The fate of the Indian lithosphere beneath western Tibet: Upper mantle elastic wave speed structure from a joint teleseismic and regional body wave tomographic study, Phys. Earth Planet. Inter., 251, 11-23.

Royden, L.H., B.C. Burchfiel and R.D. van der Hilst (2008). The Geological Evolution of the Tibetan Plateau, Science (1979), 321, 1054-1058.

Royden, L.H., B.C. Burchfiel, R.W. King, E. Wang, Z. Chen, F. Shen and Y. Liu (1997). Surface Deformation and Lower Crustal Flow in Eastern Tibet, Science (1979), 276, 788-790.

Saha, G.K., K.S. Prakasam and S.S. Rai (2020). Diversity in the peninsular Indian lithosphere revealed from ambient noise and earthquake tomography, Phys. Earth Planet. Inter., 306, 106523.

Saha, G.K., S.S. Rai, K.S. Prakasam and V.K. Gaur (2021). Distinct lithospheres in the Bay of Bengal inferred from ambient noise and earthquake tomography, Tectonophysics, 809, 228855.

Schulte-Pelkum, V., G. Monsalve, A. Sheehan, M.R. Pandey, S. Sapkota, R. Bilham and F. Wu (2005). Imaging the Indian subcontinent beneath the Himalaya, Nature, 435, 1222-1225.

Searle, M.P., R.D. Law and M.J. Jessup (2006). Crustal structure, restoration and evolution of the Greater Himalaya in Nepal-South Tibet: implications for channel flow and ductile extrusion of the middle crust, Geological Society, London, Special Publications, 268, 355-378.

Searle, M.P. and A.J. Rex (1989). Thermal model for the Zanskar Himalaya, J. Metamorph. Geol., 7, 127-134.

Searle, M.P., R.L. Simposn, R.D. Law, R.R. Parrish and D.J. Waters (2003). The structural geometry, metamorphic and magmatic evolution of the Everest massif, High Himalaya of Nepal-South Tibet, J. Geol. Soc. London, 160, 345-366.

Searle, M.P. and A.G. Szulc (2005). Channel flow and ductile extrusion of the high Himalayan slab-the Kangchenjunga-Darjeeling profile, Sikkim Himalaya, J. Asian Earth. Sci., 25, 173-185.

Searle, M.P., R.F. Weinberg and W.J. Dunlap (1998). Transpressional tectonics along the Karakoram fault zone, northern Ladakh: constraints on Tibetan extrusion, Geological Society, London, Special Publications, 135, 307-326.

Searle, M.P., J.R. Elliott, R.J. Phillips and S.-L. Chung (2011). Crustal-lithospheric structure and continental extrusion of Tibet, J. Geol. Soc. London, 168, 633-672.

Sun, X., X. Song, S. Zheng, Y. Yang and M.H. Ritzwoller (2010). Three dimensional shear wave velocity structure of the crust and upper mantle beneath China from ambient noise surface wave tomography, Earthq. Sci., 23, 449-463.

Takei, Y. (2000). Acoustic properties of partially molten media studied on a simple binary system with a controllable dihedral angle, J.Geophys. Res. Solid Earth, 105, 16665-16682.

Tapponnier, P. and P. Molnar (1977). Active faulting and tectonics in China, J. Geophys. Res., 82, 2905-2930.

Tapponnier, P. and P. Molnar (1976). Slip-line field theory and large-scale continental tectonics. Nature, 264, 319-324.

Tapponnier, P., G. Peltzer, A.Y. Le Dain, R. Armijo and P. Cobbold (1982). Propagating extrusion tectonics in Asia: New insights from simple experiments with plasticine, Geology, 10, 611.

Tilmann, F. and J. Ni (2003). Seismic Imaging of the Downwelling Indian Lithosphere Beneath Central Tibet, Science (1979), 300, 1424-1427.

Unsworth, M.J., A.G. Jones, W. Wei, G. Marquis, S.G. Gokarn and J.E. Spratt (2005). Crustal rheology of the Himalaya and Southern Tibet inferred from magnetotelluric data, Nature, 438, 78-81.

Watanabe, T. (1993). Effects of water and melt on seismic velocities and their application to characterization of seismic reflectors, Geophys Res Lett, 20, 2933-2936.

Wittlinger, G., J. Vergne, P. Tapponnier, V. Farra, G. Poupinet, M. Jiang, H. Su, G. Herquel and A. Paul, (2004). Teleseismic imaging of subducting lithosphere and Moho offsets beneath western Tibet, Earth. Planet. Sci. Lett., 221, 117-130.

Yang, Y. et al. (2010). Rayleigh wave phase velocity maps of Tibet and the surrounding regions from ambient seismic noise tomography, Geochem. Geophys. Geosys., 11, no. 8, n/a-n/a.

Yin, A. and T.M. Harrison (2000). Geologic Evolution of the Himalayan-Tibetan Orogen, Annu. Rev. Earth Planet. Sci., 28, 211-280.

Zhang, Z., Y. Deng, J. Teng, C. Wang, R. Gao, Y. Chen and W. Fan (2011). An overview of the crustal structure of the Tibetan plateau after 35 years of deep seismic soundings, J. Asian Earth Sci., 40, 977-989.

Zhang, Z., Y. Wang, G.A. Houseman, T. Xu, Z. Wu, X. Yuan, Y. Chen, X. Tian, Z. Bai and J. Teng (2014). The Moho beneath western Tibet: Shear zones and eclogitization in the lower crust, Earth Planet. Sci. Lett., 408, 370-377.

Zhao, J. et al. (2010). The boundary between the Indian and Asian tectonic plates below Tibet, Proceedings of the National Academy of Sciences, 107, 11229-11233.

***CORRESPONDING AUTHOR: Utpal SAIKIA**,
Department of Earth & Climate Science, Indian Institute of Science Education & Research- Tirupati, Tirupati-517507, India
e-mail: ngriutpal@gmail.com